

# Assignment 4: Classical Molecular Dynamics of Silver Iodide

Sylvain Mortgat

June 2, 2025

## 1 Introduction

Silver iodide (AgI) is a fast-ion conductor that exhibits a temperature-driven phase transition between a low-temperature solid phase – where both silver and iodine atoms occupy well-defined lattice positions – and a high-temperature superionic phase, in which silver ions become highly mobile while the iodide sublattice remains relatively fixed [1, 2]. Due to this property, superionic conductors find applications in a variety of domains, for instance in solid electrolytes [3] or photographic materials [4].

This report focuses on the study of silver iodide using classical molecular dynamics simulations. In Section 2, convergence tests are performed to optimize simulation parameters. First, energy conservation is evaluated as a function of the integration timestep, followed by an analysis of temperature fluctuations with respect to supercell size. The production time is then determined by studying the decay of the velocity autocorrelation function (VAF). With optimized parameters, Section 3 examines the structural and dynamical properties of AgI. The radial distribution function and mean square displacement are computed to characterize the local atomic environment and diffusion behaviour at varying temperatures. Finally, the temperature-dependent silver diffusion coefficient is compared to the Arrhenius law [5, 6], yielding the activation energy for diffusion. All molecular dynamics simulations are performed using the LAMMPS framework [7], with a Morse-Coulomb hybrid interatomic potential developed by Niu et al. [8] that uses parameters derived from DFT calculations. All analysis scripts used in this study are openly accessible on [GitHub](https://github.com/sylvainshan/MSE-468-Atomistic-and-Quantum-Simulations-of-Materials/tree/main/lab4).<sup>1</sup>

## 2 Convergence Analysis and Parameter Optimization

### 2.1 Methodology

The system is initialized by sampling velocity components uniformly. Periodic boundary conditions are applied using a cubic supercell of size  $n \times n \times n$

with a lattice constant of 5.37 Å.<sup>2</sup> Following initialization, equilibration is performed in the canonical (NVT) ensemble for  $t_{\text{eq}}$  picoseconds to allow the system to thermalize at the target temperature and to ensure that the velocity distribution converge toward a Maxwell-Boltzmann distribution. Once equilibration is achieved, the simulation is switched to the microcanonical (NVE) ensemble and propagated for an additional  $t_{\text{sim}}$  picoseconds to study the system's dynamics under energy-conserving conditions. All observables are measured during the NVE production phase.

**Integration timestep.** A suitable timestep ( $\Delta t$ ) is determined by monitoring total energy fluctuations in a 32-atom ( $2 \times 2 \times 2$ ) AgI supercell at 800 K. The timestep is varied from 0.00005 ps to 0.05 ps. For each simulation, equilibration and production durations are set to  $t_{\text{eq}} = 5$  ps and  $t_{\text{sim}} = 6$  ps respectively. The total energy is computed every 0.1 ps during production, yielding 60 measurements per run. From these measurements, the standard deviation of the total energy per atom over time,  $\sigma_E$ , is computed. Convergence is achieved when  $\sigma_E$  falls below  $10^{-5}$  eV/atom. The corresponding timestep is adopted for subsequent simulations.

**Supercell size.** The appropriate supercell size is determined by analyzing temperature fluctuations across systems ranging from  $2 \times 2 \times 2$  (32 atoms) to  $10 \times 10 \times 10$  (2000 atoms) at both 293 K and 800 K. For each supercell, identical simulation protocols are performed with 5 ps NVT equilibration followed by 6 ps NVE production, and temperature sampled every 0.1 ps. Convergence is established when the relative temperature fluctuations  $\sigma_T/T$  fall below 3%, where  $\sigma_T$  represents the standard deviation of instantaneous temperature measurements during production. Additionally, the scaling relationship between  $\sigma_T/T$  and system size  $N$  is examined. According to statistical mechanics it should follow  $\sigma_T/T \sim N^{-1/2}$  [9]. This prediction is verified by fitting power-laws to the data using the `lmfit` package [10].

<sup>1</sup>Full link: <https://github.com/sylvainshan/MSE-468-Atomistic-and-Quantum-Simulations-of-Materials/tree/main/lab4>

<sup>2</sup>Although the lattice constant should ideally be optimized for each temperature and pressure condition, this is not the focus of the present study.

**Equilibration time.** An additional simulation is performed using the optimized timestep and supercell size established before, and an equilibration duration of  $t_{\text{eq}} = 5$  ps. Atomic velocities are recorded both at the initial time  $t = 0$  ps and after the equilibration period  $t = 5$  ps. This post-equilibration analysis serves as a sanity check to verify the adequacy of the chosen equilibration time.

**Production time.** Accurate estimation of physical quantities in MD simulations requires averaging over statistically independent configurations. To ensure meaningful results for dynamical observables, it is essential that atomic trajectories become sufficiently decorrelated over time. This defines a characteristic timescale  $t_{\text{decor}}$  beyond which the system has effectively lost memory of its initial state. One way of estimating  $t_{\text{decor}}$  involves evaluating the velocity autocorrelation function (VAF), which quantifies how long particle velocities remain correlated. The VAF is defined as the time- and ensemble-averaged scalar product of particle velocities:

$$\text{VAF}(t) = \frac{1}{3N} \sum_{i=1}^N \langle \mathbf{v}_i(t + \tau) \cdot \mathbf{v}_i(\tau) \rangle_{\tau}, \quad (1)$$

where  $\langle \cdot \rangle_{\tau}$  denotes a time average, and  $N$  is the total number of atoms. The normalized velocity autocorrelation function (NVAF) is then given by  $\text{VAF}(t)/\text{VAF}(0)$ , which satisfies  $\text{NVAF}(0) = 1$  and decays toward zero as dynamical correlations are lost. The decorrelation time  $t_{\text{decor}}$  is then defined as the time after which the NVAF exhibits small-amplitude fluctuations around zero. To estimate  $t_{\text{decor}}$ , the NVAF is computed at 293 K using the optimized timestep and supercell size, with the same equilibration and production times as in previous tests. The procedure is repeated at 800 K for comparison. Since thermal fluctuations increase with temperature, velocity correlations decay more rapidly at higher temperatures. Therefore, the decorrelation time estimated at the lowest temperature (293 K) provides a conservative upper bound that is suitable for all subsequent simulations. Additionally, the VAF is related to the average kinetic energy through

$$\begin{aligned} \text{VAF}(0) &= \frac{1}{3N} \sum_{i=1}^N \langle \|\mathbf{v}_i(\tau)\|^2 \rangle_{\tau} \\ &= \frac{1}{3N} \sum_{i=1}^N \left\langle \frac{2E_{\text{kin},i}(\tau)}{m_i} \right\rangle_{\tau}. \end{aligned} \quad (2)$$

Splitting the sum over the two species and denoting  $N_{\text{at}}$  the number of atoms of each type ( $N = N_{\text{Ag}} + N_{\text{I}}$  and  $N_{\text{Ag}} = N_{\text{I}}$ , so  $N = 2N_{\text{at}}$ ), one obtains

$$\text{VAF}(0) = \frac{2}{3N} \sum_{i=1}^{N_{\text{at}}} \frac{\langle E_{\text{kin},i}^{(\text{Ag})} \rangle_{\tau}}{m_{\text{Ag}}} + \frac{\langle E_{\text{kin},i}^{(\text{I})} \rangle_{\tau}}{m_{\text{I}}}. \quad (3)$$

Assuming equipartition, each atom has an average kinetic energy  $\langle E_{\text{kin},i} \rangle_{\tau} = \frac{3}{2}k_B T$ , independent of species. This leads to

$$\text{VAF}(0) = \frac{k_B T}{N} \left( \frac{N_{\text{Ag}}}{m_{\text{Ag}}} + \frac{N_{\text{I}}}{m_{\text{I}}} \right). \quad (4)$$

Using  $N = 2N_{\text{at}}$ , Equation (4) simplifies to

$$\text{VAF}(0) = \frac{k_B T}{2} \left( \frac{1}{m_{\text{Ag}}} + \frac{1}{m_{\text{I}}} \right). \quad (5)$$

Equation (3) provides a numerical estimate of  $\text{VAF}(0)$  based on the kinetic energies extracted from simulation data, whereas Equation (5) yields a theoretical prediction derived from the equipartition theorem. Comparing both values for a given trajectory allows for a consistency check between the simulated dynamics and the expected thermodynamic behavior.

## 2.2 Results and Discussion

**Integration timestep and supercell size.** The convergence analysis of both timestep and supercell size is presented in Figure 1. Figure 1a demonstrates the timestep dependence of the standard deviation in total energy per atom, which exhibits two distinct regimes. First, a systematic decrease of  $\sigma_E$  with reducing timestep down to 0.0005 ps. Then, a plateau where further timestep reduction yields no reduction of  $\sigma_E$ . This plateau represents the numerical limit of our integration scheme. The system achieves convergence at  $\Delta t = 0.004$  ps, where  $\sigma_E$  approaches the threshold criterion of  $10^{-5}$  eV/atom. A more conservative timestep of  $\Delta t = 0.002$  ps is adopted for subsequent production runs. This choice provides a larger margin below the convergence threshold while maintaining reasonable computational efficiency.

The temperature fluctuation analysis reveals distinct behaviors for the two studied temperatures (Fig. 1b). At 800 K, a monotonic decrease of  $\sigma_T/T$  is observed across the entire range of supercell sizes. For room temperature (293 K), this decrease is only maintained up to size 6, beyond which  $\sigma_T/T$  plateaus at the convergence threshold of 3%. The power-law scaling analysis is consequently performed differently for each temperature regime. For 293 K data, only sizes from 2 to 6 are fitted whereas all data points are included for 800 K. In both cases, the extracted exponents ( $-0.52 \pm 0.04$  at 293 K and  $-0.50 \pm 0.04$  at 800 K) are found to be in agreement with the theoretically predicted  $-0.5$  scaling that falls within the 95% confidence intervals. Based on these results, a supercell size of  $6 \times 6 \times 6$  (864 atoms) is selected for all subsequent simulations, as it satisfies the convergence criterion at both temperatures.

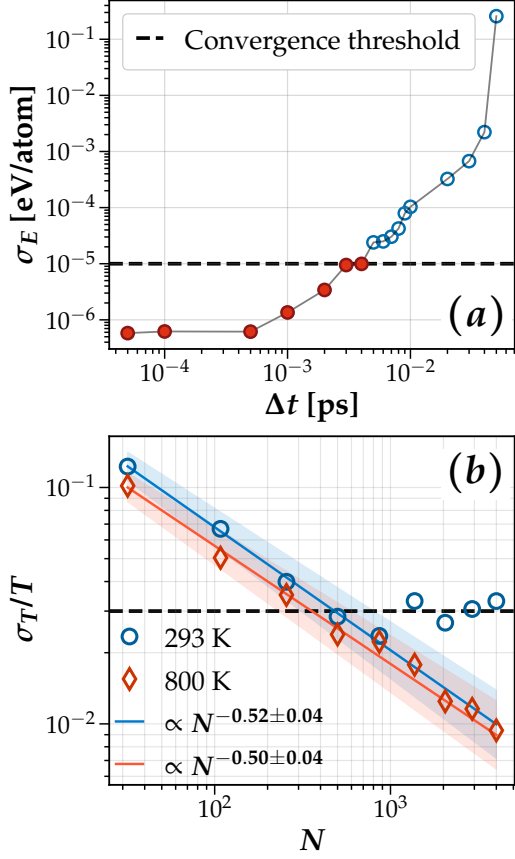


**Figure 1.** (a) Standard deviation of total energy fluctuations per atom as a function of integration timestep at 800 K. Red filled (blue hollow) markers indicate converged (non-converged) timesteps. The black dashed line represents the convergence threshold of  $10^{-5}$  eV per atom. (b) Relative temperature fluctuations with respect to the number of atoms inside the supercell at 293 K and 800 K. Solid lines represent power-law fits with 95% confidence intervals (shaded regions). The exponents of approximately  $-0.5$  are consistent with the expected scaling from statistical physics. The horizontal dashed line indicates the 3% convergence threshold used to determine the minimum required system size.

**Equilibration time.** The thermalization of velocity distributions during equilibration is illustrated in Figure 2. At  $t = 0$  ps (left panel), velocity components are approximately uniformly distributed, as expected from the initial conditions. After 5 ps of evolution in the canonical (NVT) ensemble, the distributions converge toward their theoretical forms: Gaussian profiles for the individual velocity components ( $v_x, v_y, v_z$ ) with standard deviation of  $k_B T/m$ , and a Maxwell-Boltzmann distribution for the norm of the velocity  $\|\mathbf{v}\|$ . The temperature dependence is clearly visible, with distributions at 800 K being broader than those at 293 K. These observations confirm that thermal equilibrium is effectively reached within the chosen equilibration time. The corresponding figure

for silver atoms (Fig. A1) is provided in Appendix A.

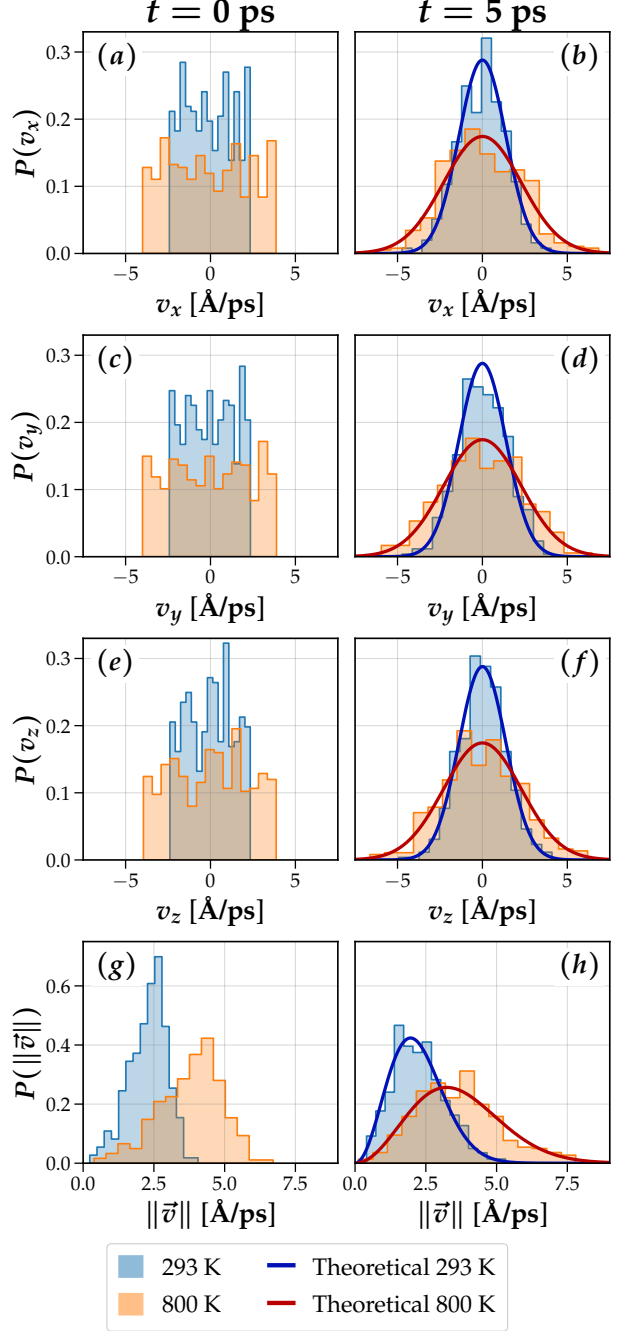


**Figure 2.** Velocity distributions for Iodine atoms at 293 K (blue) and 800 K (orange). Initial distributions (left column) and equilibrated distributions after 5 ps of NVT dynamics (right column) are shown for: (a, b)  $v_x$  component (c, d)  $v_y$  component (e, f)  $v_z$  component (g, h) norm  $\|\mathbf{v}\|$ . Theoretical Gaussian distributions for velocity components (a-f) and Maxwell-Boltzmann distributions for the norm (g, h) are illustrated with solid lines.

**Production time.** The normalized velocity autocorrelation functions for AgI at various temperatures are presented in Figure 3. In addition to the aforementioned temperatures (293 K and 800 K), an additional simulation at 100 K is included to demonstrate the temperature dependence of velocity correlations. As expected, slower decorrelation is observed for the lowest temperature, where the curve exhibits slightly more pronounced oscillations. The NVAf curves for 293 K and 800 K, display similar convergence behaviors, with both returning to zero at approximately 0.2 ps before oscillating with small amplitude around the zero value. The magnified view in the inset highlights these small fluctuations in the region between 0.1 ps and 0.7 ps. Based on these observations, the decorrelation time for the system is defined as  $t_{\text{decor}} = 0.2$  ps. Configurations separated by this interval can be considered statistically independent for the calculation of dynamical observables.

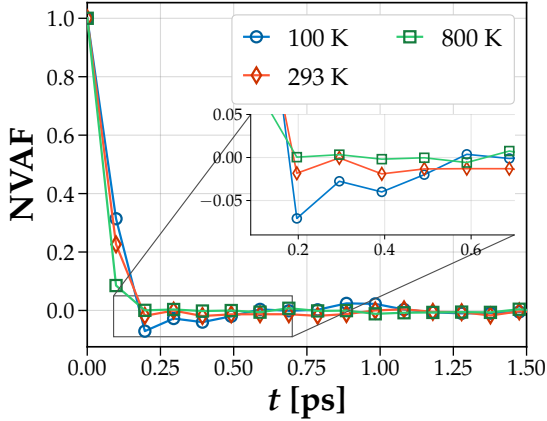


**Figure 3.** Normalized velocity autocorrelation functions (NVAf) for AgI as a function of time at three different temperatures (100 K, 293 K, and 800 K). The inset provides a magnified view of the region between 0.1 ps and 0.7 ps. The decorrelation time, estimated from the first zero-crossing of the NVAf at 293 K, is about 0.2 ps.

To further validate the consistency of the MD simulations, the initial value of the velocity autocorrelation function at  $t = 0$  (Eq.(3)) is compared with its theoretical prediction (Eq.(5)). For the trajectory at 800 K, the estimated value from simulation data is found to be  $5.65 \times 10^4 \text{ m}^2/\text{s}^2$ , while the theoretical prediction yields  $5.70 \times 10^4 \text{ m}^2/\text{s}^2$ . These values differ by less than 1%, their agreement confirms that the system properly satisfies the equipartition theorem. This correspondence serves as an important verification that the velocities are correctly sampled from the appropriate Maxwell-Boltzmann distribution and that the system has attained proper thermodynamic equilibrium before the analysis of dynamical properties.

### 3 Structural and Dynamical Properties of Silver Iodide

The structural and dynamical characteristics of silver iodide in its superionic phase are investigated in this section. All simulations are performed within the canonical ensemble. Unless stated otherwise, simulations are performed using a time step of 0.002 ps, a supercell size of  $6 \times 6 \times 6$ , and equilibration and production times of 5 ps and 6 ps, respectively. The emergence of the superionic phase is demonstrated through analysis of the radial distribution function (RDF). The temperature dependence of ionic diffusion is quantified by computing diffusion coefficients and extracting the activation energy via Arrhenius-law fitting.

#### 3.1 Methodology

**Radial Distribution Function.** The structural properties of AgI are characterized by evaluating the RDF,  $g(r)$ , for both silver and iodine ions. The RDF is computed separately for each species at room temperature (293 K) and at a low temperature (10 K). It is defined as the ratio of the average local number density  $\rho(r)$  of particles at a distance  $r$ , to the bulk density of particles  $\rho = N/V$ . Let  $dn(r)$  denote the average number of atoms located within a spherical shell of radius  $r$  and thickness  $dr$  whose volume is  $dV = 4\pi r^2 dr$ . Then, the RDF is defined as:

$$g(r) = \frac{dn(r)/dV}{N/V} = \frac{dn(r)}{4\pi r^2 dr N/V}. \quad (6)$$

In practice,  $dn(r)$  is obtained by discretizing the range of interatomic distances into  $M$  bins of width  $dr$  and counting the number of atomic pairs whose separations fall within each interval  $[idr, (i+1)dr]$ , where  $i \in \{0, 1, \dots, M-1\}$ . The result is averaged over the simulation trajectory to improve statistical accuracy.

**Mean square displacement and Diffusion coefficients.** In the superionic phase of AgI, iodine atoms remain arranged in a solid-like structure, whereas silver ions exhibit high mobility. This ionic diffusion can be quantified by computing the diffusion coefficient  $D$ , which is related to the time derivative of the mean square displacement (MSD). In three dimensions, this relation is given by the Einstein relation:

$$D = \frac{1}{6} \lim_{t \rightarrow \infty} \frac{d}{dt} \text{MSD}(t), \quad (7)$$

where the MSD is defined as:

$$\text{MSD}(t) = \frac{1}{N} \sum_{i=1}^N \langle \|\mathbf{R}_i(t) - \mathbf{R}_i(0)\|^2 \rangle. \quad (8)$$

Here,  $\mathbf{R}_i(t)$  denotes the position of particle  $i$  at time  $t$ , and  $\langle \cdot \rangle$  indicates a time average over the trajec-

tory. In practice,  $D$  is obtained by performing a linear fit to the MSD curve,<sup>3</sup> where the displacement increases linearly with time. This analysis is carried out for nine temperatures ranging from 293 K to 800 K. A longer production run of 20 ps is employed. Diffusion coefficients are extracted for each temperature.

**Activation energy.** The temperature dependence of ionic diffusion in AgI is analyzed using the Arrhenius law, which relates the diffusion coefficient to the activation energy for diffusion. Empirically, the diffusion coefficient follows an exponential relationship with temperature:

$$D = D_0 \exp\left(-\frac{E_a}{RT}\right), \quad (9)$$

where  $D_0$  is the pre-exponential factor,  $E_a$  is the molar activation energy,  $R$  is the universal gas constant, and  $T$  is the temperature. Taking the natural logarithm of Equation (9) yields a linear relationship:

$$\log D = \log D_0 - \frac{E_a}{R} \frac{1}{T} \quad (10)$$

that allows the extraction of  $D_0$  and  $E_a$  by performing a linear regression of  $\ln D$  versus  $1/T$ . This analysis is applied to the six diffusion coefficients obtained by fitting the mean square displacement. The parameters  $D_0$  and  $E_a$  and their corresponding uncertainties, which are reported as 95% confidence intervals, are obtained from the fit.

### 3.2 Results and Discussion

**Radial distribution function.** Figure 4 illustrates the structural properties of silver iodide, as characterized by the radial distribution functions at 10 K and 293 K. At 10 K, both silver and iodine ions exhibit sharp, well-defined RDF peaks, with the first coordination shell appearing at approximately 5 Å. These pronounced peaks reflect the long-range order characteristic of crystalline solids. In contrast, at 293 K, the two species display different behaviors. The iodine RDF maintains solid-like characteristics with pronounced peaks and valleys, whereas the silver RDF transforms to a liquid-like profile characterized by a broad initial peak at 2.5 Å, followed by rapid damping toward unity. This contrast provides evidence of the superionic phase of AgI at room temperature, where the iodine sublattice remains ordered while silver ions are characterized by a greater mobility. The observed behavior suggests significantly higher diffusion coefficients for silver compared to iodine.

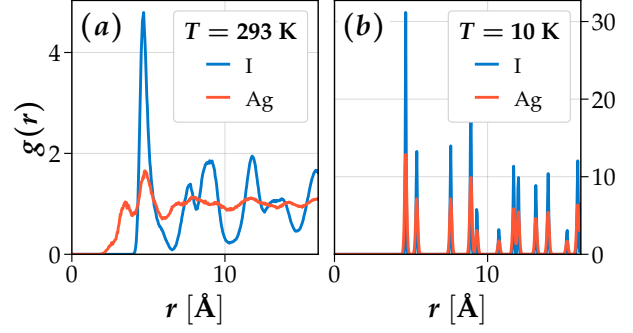


**Figure 4.** Radial distribution function of AgI are shown at two temperatures: (a) 293 K and (b) 10 K. The RDFs of iodine (I) and silver (Ag) are represented by blue and orange curves, respectively.

**Diffusion coefficients.** The mean square displacement curves for silver and iodine ions at various temperatures are presented in Figure 5, where distinct dynamic behaviors between the two ionic species are clearly observed. For iodine atoms (Fig. 5a), the MSD values remain nearly constant (approximately 0.5 Å<sup>2</sup>) across most temperatures, with a slight increase observed only at room temperature. This behavior confirms the stability of the iodine sublattice throughout the studied temperature range. In contrast, silver ions (Fig. 5b) exhibit pronounced diffusive behavior characterized by linear MSD growth with time at all temperatures. The slopes of these curves are found to increase systematically with temperature, indicating larger ionic mobility at elevated temperatures. Diffusion coefficients are extracted by fitting the linear regime of the MSD curves between 8 ps and 20 ps to focus on the asymptotic behavior. The validity of this approach is confirmed by the agreement between experimental data and linear fits, as illustrated for

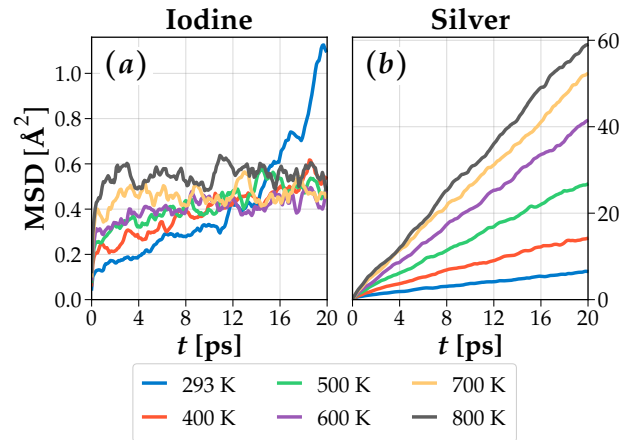


**Figure 5.** Mean square displacement as a function of time for (a) iodine and (b) silver atoms in AgI at various temperatures ranging from 293 K to 800 K.

<sup>3</sup>Again, using the `lmfit` package.



three representative temperatures in Figure A2 presented in Appendix A. The calculated diffusion coefficients, presented in Table 1, exhibit agreement with literature values within the same order of magnitude while showing systematic deviations. For instance, the non-equilibrium molecular dynamics results reported by Carvalho et al. [2] exceed our values by 40%, 11%, and 20% at 450 K, 550 K, and 650 K, respectively.

$T$ [K]	$D \cdot 10^{-5}$ [cm <sup>2</sup> /s]	$D_{\text{ref}} \cdot 10^{-5}$ [cm <sup>2</sup> /s]
293	$0.48 \pm 0.03$	—
400	$1.09 \pm 0.11$	—
450	$1.48 \pm 0.11$	2.47 [11], 2.25 [12], 2.46 $\pm$ 0.16 [2]
500	$2.22 \pm 0.14$	—
550	$2.76 \pm 0.16$	3.82 [11], 4.73 [13], 3.46 [12], 3.1 $\pm$ 0.2 [2]
600	$3.38 \pm 0.19$	—
650	$3.69 \pm 0.19$	5.48 [11], 4.82 [12] 4.6 $\pm$ 0.5 [2]
700	$4.3 \pm 0.3$	—
800	$4.9 \pm 0.3$	—

**Table 1.** Diffusion coefficients of silver ( $D$ ) determined from linear fits to MSD curves in Figure 5. Uncertainties in this work represent 95% confidence intervals. Literature values ( $D_{\text{ref}}$ ) are included where available, with reported uncertainties when provided in the original sources.

**Activation energy.** The temperature dependence of silver ion diffusion is illustrated in Figure 6, where the Arrhenius relationship is evaluated by plotting the logarithm of the diffusion coefficient against the inverse temperature. An excellent fit to the experimental data is observed, with a coefficient of determination  $R^2 = 0.99$ . From this analysis, the pre-exponential factor  $D_0$  is determined to be  $(21.3 \pm 1.9) \times 10^{-5}$  cm<sup>2</sup>/s, while the activation energy  $E_a$  is found to be  $(2200 \pm 120)$  cal/mol. The activation energy corresponds to approximately  $(0.098 \pm 0.005)$  eV per silver atom. As summarized in Table 2, these values compare favorably with those reported in the literature. The activation energy shows remarkable agreement with the value reported by Kvist and Tärneberg [14], with only a 0.5% relative difference. The pre-exponential factor also aligns well with previous studies, particularly with Niu et al. [8] where the relative difference is only 6%. This close agreement is expected, as the present work utilizes the potential developed by Niu et al. [8]. The strong linearity of the Arrhenius plot confirms that silver ion diffusion in AgI follows a thermally activated mechanism throughout the investigated temperature range.

Source	$D_0 \cdot 10^{-5}$ [cm <sup>2</sup> /s]	$E_a$ [cal/mol]	Relative error[%]
This work	$21.3 \pm 1.9$	$2200 \pm 120$	—
Niu et al. [8]	22.57	2580	6   17
Kvist [14]	16.62	2190	22   0.5
Wuensch [15]	—	1153	—   48

**Table 2.** Comparison of Arrhenius parameters for silver ion diffusion in AgI.

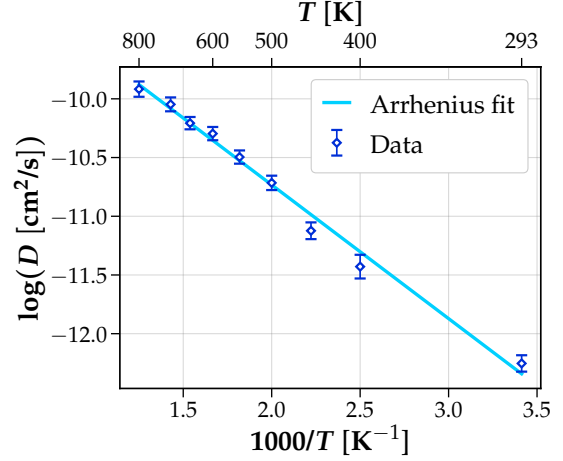


**Figure 6.** Temperature dependence of silver ion diffusion in AgI. Blue diamond markers represent diffusion coefficients extracted from simulations across temperatures ranging from 293 K to 800 K, with error bars indicating 95% confidence intervals derived from linear MSD fits. The cyan line shows the Arrhenius fit (Eq.(9), yielding an activation energy of 2200 cal/mol (0.098 eV per atom).

## References

- [1] Trevor P. Bailey and Ctirad Uher. Potential for superionic conductors in thermoelectric applications. *Current Opinion in Green and Sustainable Chemistry*, 4:58–63, 2017. ISSN 2452-2236. doi: <https://doi.org/10.1016/j.cogsc.2017.02.007>. URL <https://www.sciencedirect.com/science/article/pii/S2452223616300827>. 4 Novel materials for energy production and storage 2017.
- [2] Alexandra Carvalho, Suchit Negi, and Antonio H. Castro Neto. Direct calculation of the ionic mobility in superionic conductors. *Scientific Reports*, 12(1):19930, Nov 2022. ISSN 2045-2322. doi: [10.1038/s41598-022-21561-1](https://doi.org/10.1038/s41598-022-21561-1). URL <https://doi.org/10.1038/s41598-022-21561-1>.
- [3] Jian Gao, Yu-Sheng Zhao, Si-Qi Shi, and Hong Li. Lithium-ion transport in inorganic solid state electrolyte\*. *Chinese Physics B*, 25(1):018211, dec 2015. doi: [10.1088/1674-1056/25/1/018211](https://doi.org/10.1088/1674-1056/25/1/018211). URL <https://dx.doi.org/10.1088/1674-1056/25/1/018211>.
- [4] Kyle E. Jacobs and Placid M. Ferreira. Painting and direct writing of silver nanostructures on phosphate glass with electron beam irradiation. *Advanced Functional Materials*, 25(33):5261–5268, 2015. doi: <https://doi.org/10.1002/adfm.201501965>. URL <https://advanced.onlinelibrary.wiley.com/doi/abs/10.1002/adfm.201501965>.
- [5] Svante Arrhenius. Über die reaktionsgeschwindigkeit bei der inversion von rohrzucker durch säuren. *Zeitschrift für Physikalische Chemie*, 4U(1):226–248, 1889. doi: [doi:10.1515/zpch-1889-0416](https://doi.org/10.1515/zpch-1889-0416). URL <https://doi.org/10.1515/zpch-1889-0416>.

- [6] Keith J. Laidler. The development of the arrhenius equation. *Journal of Chemical Education*, 61(6):494, Jun 1984. ISSN 0021-9584. doi: [10.1021/ed061p494](https://doi.org/10.1021/ed061p494). URL <https://doi.org/10.1021/ed061p494>.
- [7] A. P. Thompson, H. M. Aktulga, R. Berger, D. S. Bolintineanu, W. M. Brown, P. S. Crozier, P. J. in 't Veld, A. Kohlmeyer, S. G. Moore, T. D. Nguyen, R. Shan, M. J. Stevens, J. Tranchida, C. Trott, and S. J. Plimpton. LAMMPS - a flexible simulation tool for particle-based materials modeling at the atomic, meso, and continuum scales. *Comp. Phys. Comm.*, 271:108171, 2022. doi: [10.1016/j.cpc.2021.108171](https://doi.org/10.1016/j.cpc.2021.108171).
- [8] Hongwei Niu, Yuhang Jing, Yi Sun, and Narayana R. Aluru. Ab initio based interionic potential for silver iodide. *Solid State Ionics*, 325:102–111, 2018. ISSN 0167-2738. doi: <https://doi.org/10.1016/j.ssi.2018.07.027>. URL <https://www.sciencedirect.com/science/article/pii/S016727381830331X>.
- [9] J. Hickman and Y. Mishin. Temperature fluctuations in canonical systems: Insights from molecular dynamics simulations. *Phys. Rev. B*, 94:184311, Nov 2016. doi: [10.1103/PhysRevB.94.184311](https://doi.org/10.1103/PhysRevB.94.184311). URL <https://link.aps.org/doi/10.1103/PhysRevB.94.184311>.
- [10] Matthew Newville, Renee Otten, Andrew Nelson, Till Stensitzki, Antonino Ingargiola, Daniel Allan, Austin Fox, Faustin Carter, and Michal Rawlik. Lmfit: Non-linear least-squares minimization and curve-fitting for python, March 2025. URL <https://doi.org/10.5281/zenodo.15014437>.
- [11] K. Funke and R. Hackenberg. Ionen-halleffekt in  $\alpha$ -agi. *Berichte der Bunsengesellschaft für physikalische Chemie*, 76(9):883–885, 1972. doi: <https://doi.org/10.1002/bbpc.19720760904>. URL <https://onlinelibrary.wiley.com/doi/abs/10.1002/bbpc.19720760904>.
- [12] K. Funke. Agi-type solid electrolytes. *Progress in Solid State Chemistry*, 11:345–402, 1976. ISSN 0079-6786. doi: [https://doi.org/10.1016/0079-6786\(76\)90001-7](https://doi.org/10.1016/0079-6786(76)90001-7). URL <https://www.sciencedirect.com/science/article/pii/0079678676900017>.
- [13] Y. J. Liou, R. A. Hudson, S. K. Wonnell, and L. M. Slifkin. Ionic hall effect in crystals: Independent versus cooperative hopping in agbr and  $\alpha$ -agi. *Phys. Rev. B*, 41:10481–10485, May 1990. doi: [10.1103/PhysRevB.41.10481](https://doi.org/10.1103/PhysRevB.41.10481). URL <https://link.aps.org/doi/10.1103/PhysRevB.41.10481>.
- [14] Arnold Kvist and Roy Tärneberg. Self-diffusion of silver ions in the cubic high temperature modification of silver iodide. *Zeitschrift für Naturforschung A*, 25(2):257–259, 1970. doi: [10.1515/zna-1970-0219](https://doi.org/10.1515/zna-1970-0219). URL <https://doi.org/10.1515/zna-1970-0219>.
- [15] Bernhardt J. Wuensch. Cation distributions, bonding and transport behavior in silver and copper fast-ion conductors with simple anion packings. *Materials Science and Engineering: B*, 18(2):186–200, 1993. ISSN 0921-5107. doi: [https://doi.org/10.1016/0921-5107\(93\)90131-6](https://doi.org/10.1016/0921-5107(93)90131-6). URL <https://www.sciencedirect.com/science/article/pii/0921510793901316>.

## A Additional Figures

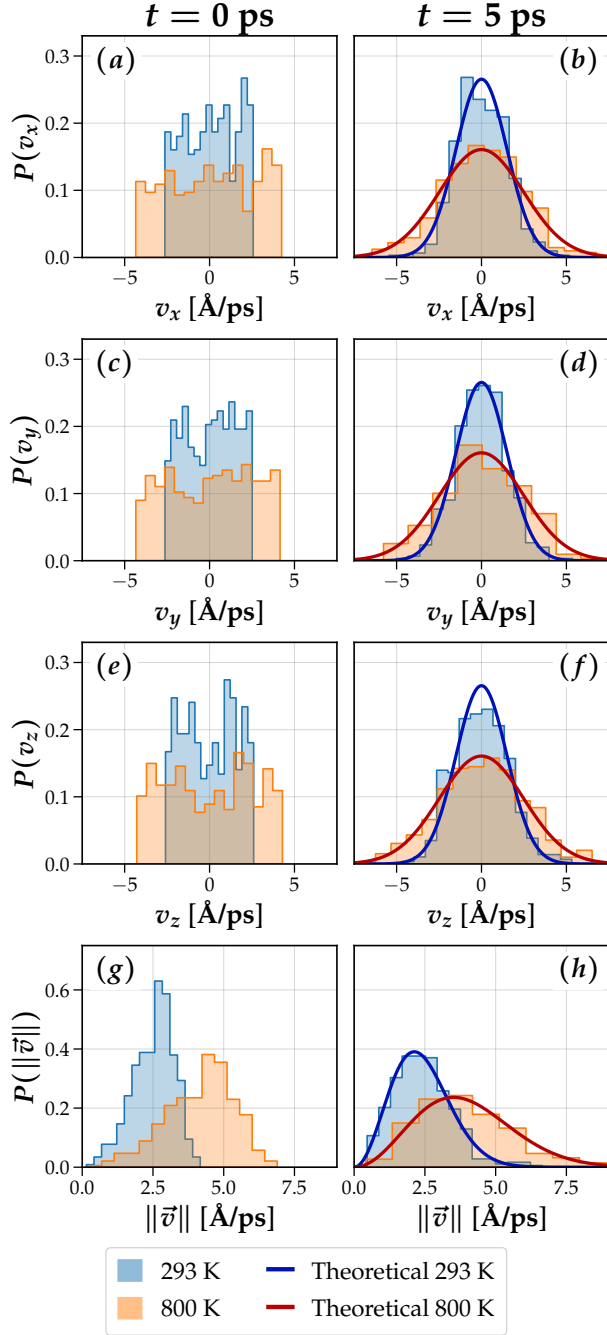


**Figure A1.** Velocity distributions for Silver atoms at 293 K (blue) and 800 K (orange). Initial distributions (left column) and equilibrated distributions after 5 ps of NVT dynamics (right column) are shown for: (a, b)  $v_x$  component (c, d)  $v_y$  component (e, f)  $v_z$  component (g, h) norm  $\|\vec{v}\|$ . Theoretical Gaussian distributions for velocity components (a-f) and Maxwell-Boltzmann distributions for the norm (g, h) are illustrated with solid lines.

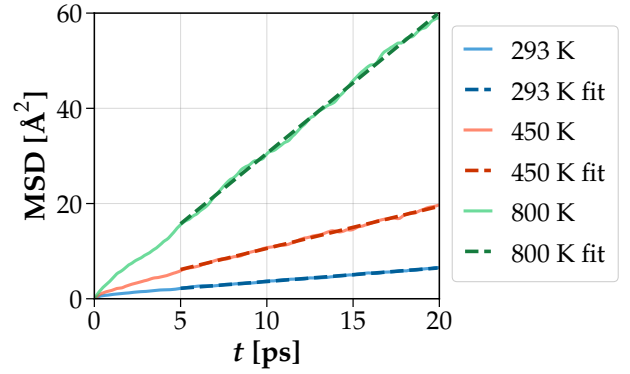


**Figure A2.** Mean square displacement of silver ions in AgI as a function of time at three representative temperatures. Solid lines represent the raw MSD data from molecular dynamics simulations. Dashed lines show the corresponding linear fits applied to the region beyond 5 ps. The linearity of MSD with time at all temperatures confirms diffusive behavior of the silver sublattice.